POLITECNICO DI TORINO
Repository ISTITUZIONALE

# Exploring lithium diffusion in LiF with machine learning potentials: from point defects to collective ring diffusion

*Original*
Exploring lithium diffusion in LiF with machine learning potentials: from point defects to collective ring diffusion / De Angelis, P., Raucci, U., Mambretti, F., Fasano, M., Chiavazzo, E., Asinari, P., Parrinello, M.. - In: NPJ COMPUTATIONAL MATERIALS. - ISSN 2057-3960. - ELETTRONICO. - 12:1(2026), pp. 1-12. [10.1038/s41524-026-02132-8]

*Availability:*
This version is available at: 11583/3012929 since: 2026-07-10T09:34:51Z

*Publisher:*
Nature Research

*Published*
DOI:10.1038/s41524-026-02132-8

*Terms of use:*

This article is made available under terms and conditions as specified in the corresponding bibliographic description in the repository

*Publisher copyright*

(Article begins on next page)

15 November 2026

# Exploring Lithium Diffusion in LiF with Machine Learning Potentials: From Point Defects to Collective Ring Diffusion (Supplementary materials)

Paolo De Angelis*[1,2], Umberto Raucci[1], Francesco Mambretti[1], Fasano Matteo[2], Eliodoro Chiavazzo[2], Pietro Asinari[2,3], and Michele Parrinello†[1]

[1]Laboratory of Atomistic Simulations, Italian Institute of Technology, Via Enrico Melen 83, Genova, 16152, Italy
[2]Department of Energy "Galileo Ferraris", Politecnico di Torino, Corso Duca degli Abruzzi, 24, Turin, 10129, Italy
[3]Istituto Nazionale di Ricerca Metrologica, Strada delle Cacce 91, Torino, 10135, Italy

## Contents

**S1 Additional Methods infos** **S3**
S1.1 Active Learning sampling method . . . S3
S1.2 On-the-fly Probability Enhanced Sampling (OPES) . . . S3
S1.3 Diffusivity analysis . . . S3
S1.4 Low-barrier diffusion regime . . . S5
S1.5 SOAP-Based defect identification procedure . . . S6

**S2 Additional Analysis infos** **S9**
S2.1 MLIP: Validation . . . S9
S2.2 Vacancy Diffusion: Finite size effect quantification and FES convergence . . . S11
S2.3 Interstitial Diffusion: Finite size effect quantification . . . S14
S2.4 Ring Diffusion: Additional Electronic-Structure Analysis . . . S15
S2.5 Ring Diffusion: Additional formation mechanism analysis . . . S16

## List of Figures

S1 Comparison between Arrhenius/Kramers and Ornstein-Uhlenbeck models. . . . S5
S2 Performance assessment of the SOAP-based classification algorithm . . . S7
S3 MLIP validation: forces and energies for training and test sets . . . S9
S4 MLIP validation: phonons and equation of state . . . S10
S5 MLIP validation: migration energy profiles . . . S10
S6 Finite-size effect for vacancy diffusion . . . S11
S7 Time evolution of the collective variable . . . S12
S8 Time convergence of the free-energy surface (FES) . . . S13
S9 Finite-size effect for single-interstitial diffusion . . . S14
S10 Charge evolution during ring formation . . . S15

*Co-Corresponding author: paolo.deangelis@polito.it
†Co-Corresponding author: michele.parrinello@iit.it

S11 Bader charge density grid sensitivity . . . . . S16
S12 Finite-size dependence of the ring formation time . . . . . S17
S13 Arrhenius plot for ring formation. . . . . S17

## List of Tables

S1 SOAP settings used for Li local-environment identification. . . . . S8

# S1 Additional Methods infos

## S1.1 Active Learning sampling method

During each Active Learning round for the MLIP, we run a 3 ns- long simulation with a $3 \times 3 \times 3$ supercell, saving the trajectory every 40 steps. For every saved trajectory frame, we evaluated

$$\sigma = \max_i \left[ \sqrt{\frac{1}{N} \sum_{k=1}^{N} \left\| \mathbf{F}_i^k - \overline{\mathbf{F}}_i \right\|^2} \right], \tag{S1}$$

where $N = 4$ is the size of the MLIPs committee, $\mathbf{F}_i^k$ is the force on $i$-th atom predicted by the $k$-th MLIP, and $\overline{\mathbf{F}}_i$ is the committee average. Approximately 0.3% of the frames in the trajecctory with $\sigma \in [50, 350]$ meV/Å were selected according to the procedure described in Ref. [1], recomputed at the DFT level, and included into the updated dataset. This strategy reduces the correlation between added configurations while preferentially retaining highly informative structures that accelerate learning.

## S1.2 On-the-fly Probability Enhanced Sampling (OPES)

OPES [2, 3] reconstructs the FES $G(\mathbf{s})$ by iteratively depositing Gaussian bias kernels in the CV space $\mathbf{s}$, resulting, in the convergence limit, in the bias potential $V(\mathbf{s}) = -G(\mathbf{s})$. In OPES the kernel deposition targets the well temperature distribution $P^{tg} \propto [P(\mathbf{s})]^{\frac{1}{\gamma}}$ where $\gamma > 1$ is the bias factor. The empirical probability density $P(\mathbf{s})$ is estimated on-the-fly via instogram reweight as follow:

$$P_n(\mathbf{s}) = \frac{\sum_k^n w_k K(\mathbf{s}, \mathbf{s}_k)}{\sum_k^n w_k}, \quad w_k = \exp\left(\beta V_{k-1}(\mathbf{s}_k)\right), \tag{S2}$$

where $K$ is a Gaussian kernel, $V_{k-1}$ the bias accumulated up to step $k-1$, $\beta = (k_{\mathrm{B}}T)^{-1}$, and the weights $w_k$ reweight the histogram to equilibrium. Following this construction, the bias potential at $n$-th step is:

$$V_n(\mathbf{s}) = \left(1 - \gamma^{-1}\right) \frac{1}{\beta} \log\left(\frac{P_n(\mathbf{s})}{Z_n} + \epsilon\right) \tag{S3}$$

where $Z_n$ is the normalization factor, $\beta = (k_B T)^{-1}$ and $\epsilon = \exp\left(-\frac{\beta \Delta E}{1-\gamma^{-1}}\right) \ll 1$ is the regulariation parameter for numerical stability but also control the maximum free energy barier $\Delta E$.

## S1.3 Diffusivity analysis

To quantify lithium mobility, we first evaluated the mean-square displacement (MSD) along every trajectory and fitted it with the least-squares relation

$$\langle \mathbf{r}^2 \rangle = \alpha_0 + \alpha_1 \cdot t + \varepsilon, \tag{S4}$$

where $\langle \mathbf{r}^2 \rangle$ is the mean-square displacement, $\varepsilon$ is the error term, and $t$ denotes the elapsed simulation time. Following Einstein–Smoluchowski equation [4, 5, 6], the slope gives the diffusion coefficient, $D = \alpha_1/6$.

According to Einstein's model of Brownian motion, we also know that the diffusivity at a given temperature can be expressed as:

$$D = \frac{\delta^2}{g\,\tau}, \tag{S5}$$

where g is the dimensionality constant ($g = 6$ for the three-dimensional diffusion) $\delta$ is the diffusion hop distance and $\tau$ is the characteristic time. In a first approximation, the latter can be computed by inverting the Eyring rate equation [7] from transition state theory (TST),

$$k = \frac{1}{\tau} = \frac{t_r\, k_B T}{h}\, \exp\left(-\frac{\Delta G}{k_B T}\right), \tag{S6}$$

where $k$ is the hop frequency, $\tau$ the mean waiting time, $t_r$ the transmission coefficient, $k_B$ Boltzmann's constant, $h$ Planck's constant, and $\Delta G$ the Gibbs free energy. Assuming negligible entropy change between the initial and transition states (a reasonable approximation for point-defect diffusion) and taking $t_r = 1$, the characteristic time can be estimated with the following:

$$\tau \approx \frac{h}{k_{\mathrm{B}}T}\ \exp\!\left(\frac{\Delta E}{k_{\mathrm{B}}T}\right). \tag{S7}$$

Thus, using Eq. (S7) in Eq. (S5) we get the temperature-dependent Arrhenius-like [8] expression for the diffusivity

$$D(T) = \frac{\delta^2}{g}\frac{k_B T}{h}\ \exp\!\left(-\frac{\Delta E_a}{k_B T}\right) = D_0 \exp\!\left(-\frac{\Delta E_a}{k_B T}\right), \tag{S8}$$

where $D_0 = \delta^2 k_B T/(gh)$ is the maximum diffusivity and $\Delta E_a$ is the activation energy. The maximum diffusivity explicitly depends on temperature through the factor $k_B T/h$ and, in principle, also through the transmission coefficient $t_r$. However, in the main text, $D_0$ is treated as a temperature-independent effective maximum diffusivity when fitting MD-derived diffusivities over a limited temperature range. This standard approach incorporates the weak prefactor temperature dependence and residual entropic corrections into a single fitted constant. Therefore, $D_0$ should not be interpreted as the strict TST limit at an arbitrary temperature.

Two limitations of the above derivation should be noted. First, Eq. (S8) represents the potential-energy landscape only through the activation barrier, whereas the dynamical details of barrier crossing, such as recrossing and local curvatures at the minimum and at the transition state, are effectively incorporated into a transmission coefficient. A more refined description is provided by Kramers' escape-rate theory in the Smoluchowski (overdamped) limit, which expresses the mean escape/crossing time $\tau$ [1]

After taking natural logarithms of both Eq. (S8) sides, and introducing $x = T^{-1}$, one obtains the linear form $\ln D = \beta_0 + \beta_1 x + \varepsilon$, so that the activation energy follows from the fitted slope,$E_a = -\beta_1 k_B$, while the intercept gives the prefactor $D_0 = e^{\beta_0}$.

The uncertainties for all the Arrhenius plots were estimated by assuming that the residuals of each linear regression obey a Student's t distribution $\mathcal{T}_\nu$, where $\nu$ represents the degrees of freedom of the distribution [11]. In our case, $\nu$ equals the number of simulated temperatures minus constraints of our model, which are the intercept and slope of the model ($\nu = 5 - 2 = 3$). Then the 95% confidence intervals are computed as follows:

$$\begin{aligned}\delta\left[\ln(D)\right]\left(\frac{1}{T}\right) =& t_{3,\,0.025}\cdot \\ & \sqrt{\frac{1}{n-2}\sum_{i=1}^{n}\left(\ln(D_i) - \beta_0 - \beta_1\frac{1}{T_i}\right)^2}\cdot \\ & \sqrt{\frac{1}{n} + \frac{\left(\frac{1}{T} - \left\langle\frac{1}{T}\right\rangle\right)^2}{\sqrt{\sum_{j=1}^{n}\left(\frac{1}{T_j} - \left\langle\frac{1}{T}\right\rangle\right)^2}}}.\end{aligned} \tag{S10}$$

[1] For reference, the Kramers mean escape time can be written as

$$\tau_{\mathrm{K}} = \frac{k_B T}{D\sqrt{|\omega_0\,\omega_{\mathrm{TS}}|}}\exp\!\left(\frac{\Delta E_a}{k_B T}\right), \tag{S9}$$

where $\Delta E_a$ is the activation energy, $D$ is the diffusion constant and $\omega_{0,TS} = \frac{\partial^2 E}{\partial x^2}\Big|_{0,TS}$ are the potential energy landascape curvatures at its minimum and trasmission state [9]. in terms of both the barrier height and the landscape curvatures [10, 9]. Second, the Arrhenius/Kramers exponential trend is asymptotic in the high-barrier regime ($\Delta E_a \gg k_B T$) and may deviate when the barrier becomes comparable to thermal energy. In this low-barrier regime or high thermal fluctuation ( $\Delta E_a/k_B T \to 0$), the mean escape/crossing time approaches a continuous transition to a finite free-diffusion limit. In particular, Abkenar *et al.* [9] proposed an Ornstein–Uhlenbeck (OU) model that we tested below (Subsection S1.4) to assess the magnitude of non-Arrhenius corrections for the present system.

$t_{3,0.025}$ is the cut probability 0.025 from the upper tail of Student's t distribution $\mathcal{T}_{\nu=3}$, $D_i$ is the diffusivity at temperature $T_i$, and $n = 5$ is the number of calculated diffusivity.

### S1.4 Low-barrier diffusion regime

Combining the Einstein relation for diffusion (Eq. (S5)) with either transition-state theory (Eyring; Eq. (S7)) or an escape-rate description (Kramers; Eq. (S9)) one recovers the familiar Arrhenius-type temperature dependence of the diffusivity, $D(T) \propto \exp(-\Delta E_a/k_B T)$. This law assumes a *step-like* process for the mass transport, in which long-time diffusion arises from thermally activated crossings of an energy barrier separating metastable configurations. These assumptions may break down for shallow potential-energy barriers or for sufficiently large thermal energies, i.e. where the dimensionless energy barrier $E^* \coloneqq \Delta E_a/k_B T = O(1)$.

In our study, both knock-off and ring diffusion involve a relatively small barrier ($\Delta E_a \approx 0.24\,\text{eV}$ and $\Delta E_a \approx 0.26\,\text{eV}$ respectively), which becomes progressively comparable to thermal fluctuations at the highest simulated temperatures. For example, at $T = 450\,\text{K}$ we have $E^* = \Delta E_a/(k_B T) = 6.19$ for knock-off diffusion. We therefore verify that the Arrhenius/Kramers form remains valid in the investigated operating temperature window by comparing it to the more general Ornstein-Uhlenbeck model proposed by Abkenar *et al.* [9]. The OU framework considers a particle evolving in a one-dimensional potential-energy landscape $U(x)$ with an equilibrium and transition state (or dissociated state) at $x_0$ and $x_{ST}$ respectively, and an initial condition $x$ satisfying $x_0 < x < x_{ST}$. Within this setting, the OU approach yields the mean first-passage time (MFPT) in integral form (up to a multiplicative prefactor) as [9]

$$\tau_{\text{OU}}(x) = C \int_x^{x_{ST}} \exp\left(\frac{U(y)}{k_B T}\right) \int_{x_0}^{y} \exp\left(-\frac{U(z)}{k_B T}\right) \mathrm{d}z\,\mathrm{d}y \tag{S11}$$

where $C$ is a temperature-independent scaling constant.

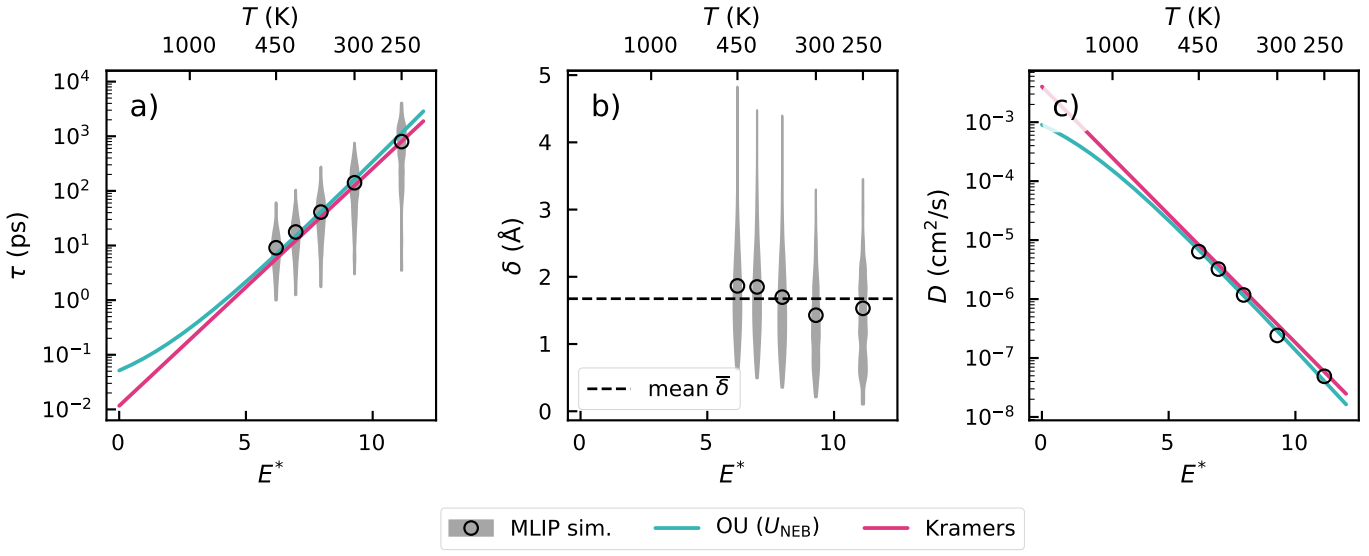



**Fig. S1:** Comparison between Arrhenius/Kramers and Ornstein-Uhlenbeck (OU) mass transport models. (a) Mean crossing time $\tau(T)$ calculated from interstitial-identity changes. (b) Characteristic displacement $\delta$ from Eq. (S5). (c) Diffusivity $D(T)$ as function of the dimensionless energy barrier $E^* \coloneqq \Delta E_a/k_B T$. Violin plots represent transition times computed from MLIP-MD trajectories, and black circles indicate mean crossing times. Solid magenta lines correspond to Kramers/Arrhenius models, solid green lines show OU model. The OU model is evaluated by numerical integration of Eq. (S11) using a spline interpolation of the DFT-NEB potential-energy profile for the knock-off pathway. Across $250 - 450\,\text{K}$, the two models difference is negligible.

In the present case, the one-dimensional potential-energy surface (PES), $U(x)$, entering Eq. (S11) is obtained directly from the DFT-NEB calculation of the knock-off diffusion show in Fig. S5. The discrete NEB energy points are interpolated by spline and the resulting profile is used for the numerical evaluation of the OU mean first-passage time. This provides a system-specific validation of the low-barrier regime based on the actual migration pathway in LiF.

To determine the scaling constant $C$ in Eq. (S11), we computed the instantaneous crossing times $\tau$ directly from all trajectories used for the single-interstitial diffusivity analysis. The individual diffusion events are identified using the ML-based procedure described in the main text: $\tau$ is defined as the waiting time between successive changes of the identified interstitial atom. The resulting distribution of crossing times is shown as a violin plot in Fig. S1.a, while the black circles denote the corresponding mean values. We then fitted the temperature dependence of the mean crossing time $\langle\tau\rangle(T)$ (black circles in Fig. S1.a) using Eq. (S11) with and NEB-DFT derived PES and assuming a starting position at the equilibrium position $x_0$ ($\tau_{\mathrm{OU}}(x = x_0)$), obtaining an excellent agreement with the simulation data (Fig. S1.a) and a consistent estimate of the scaling constant $C = 223.4\,\mathrm{s/cm^2}$. Most importantly, the MD mean crossing times remain approximately linear in the Arrhenius representation over the full investigated temperature range, without showing the pronounced nonlinearity expected in a strongly non-Arrhenius low-barrier regime.

Combining $\langle\tau\rangle(T)$ with the diffusivity $D(T)$ obtained independently from MSD slopes, we compute an effective displacement $\delta = 1.7\,\text{Å}$ via Eq. S5 (Fig. S1.b). We emphasize that $\delta$ is an effective quantity tied to the event definition, representing approximately half the length of the common reaction coordinate employed in NEB-based Transition State Theory estimates (Eq. (S8)) [12, 13]. This further demonstrates that dynamic simulations are required to more accurately estimate diffusivity.

Finally, Fig. S1.c compares Arrhenius/Kramers and OU predictions for $D(T)$ to the MLIP-MD diffusivities. Across $250-450\,\mathrm{K}$, the two models are practically indistinguishable on the scale of the data, and the difference between them remains negligible throughout the explored range. This also holds in the low-barrier regime accessed here, corresponding to $E^* > 4$.

Therefore, within the operating conditions investigated here, low-barrier non-Arrhenius corrections are negligible and do not affect the mechanistic conclusions reported in the main text.

### S1.5 SOAP-Based defect identification procedure

Lithium atoms in non-octahedral environments were identified using the Smooth Overlap of Atomic Positions (SOAP) descriptor as implemented in `DScribe` [14, 15].

The SOAP method represents the local environment around a central atom by a Gaussian-smeared neighbor density, expanded using radial basis functions and spherical harmonics. This yields a rotationally invariant descriptor known as the partial power spectrum, whose elements are defined as

$$p_{nn'l}^{Z_1Z_2} = \pi\sqrt{\frac{8}{2l+1}}\sum_m \left(c_{nlm}^{Z_1}\right)^* c_{n'lm}^{Z_2}, \tag{S12}$$

Here, $n$ and $n'$ label the radial basis functions up to $n_{\max}$, $l$ represents the angular degree up to $l_{\max}$, and $Z_1$, $Z_2$ denote the chemical species. The coefficients are obtained from $l_{\max}$, and $Z_1, Z_2$ denote the chemical species. The coefficients are obtained from

$$c_{nlm}^{Z} = \iiint_{\mathbb{R}^3} \mathrm{d}V\, g_n(r)\, Y_{lm}(\theta,\phi)\, \rho^Z(\mathbf{r}), \tag{S13}$$

where $g_n(r)$ is the radial basis function, $Y_{lm}$ are the real spherical harmonics, and the Gaussian-smeared atomic density for species $Z$ is defined as atomic density for species $Z$ is

$$\rho^Z(\mathbf{r}) = \sum_{i\in Z} \exp\left(-\frac{|\mathbf{r}-\mathbf{R}_i|^2}{2\sigma^2}\right). \tag{S14}$$

The descriptor was computed under periodic boundary conditions, considering both Li and F as chemical species, but calculations were performed exclusively for Li atoms. The specific settings employed in the production analysis are detailed in Table S1.

Initial labels for the local environments were generated in SOAP space using `DBSCAN`, clustering with parameters `eps = 0.009` and `min_samples = 5` from `scikit-learn` python library [16]. This unsupervised step identified the main clusters in the descriptor space and assigned initial octahedral and non-octahedral

labels on the training set. To accelerate frame-by-frame screening over extended trajectories, these labels trained a `HistGradientBoostingClassifier`, which provided the final production labeling. The corresponding PCA visualization of the SOAP space, along with training labels and ROC/AUC performance for both interstitial and ring cases, is presented in Supplementary Fig. S2.

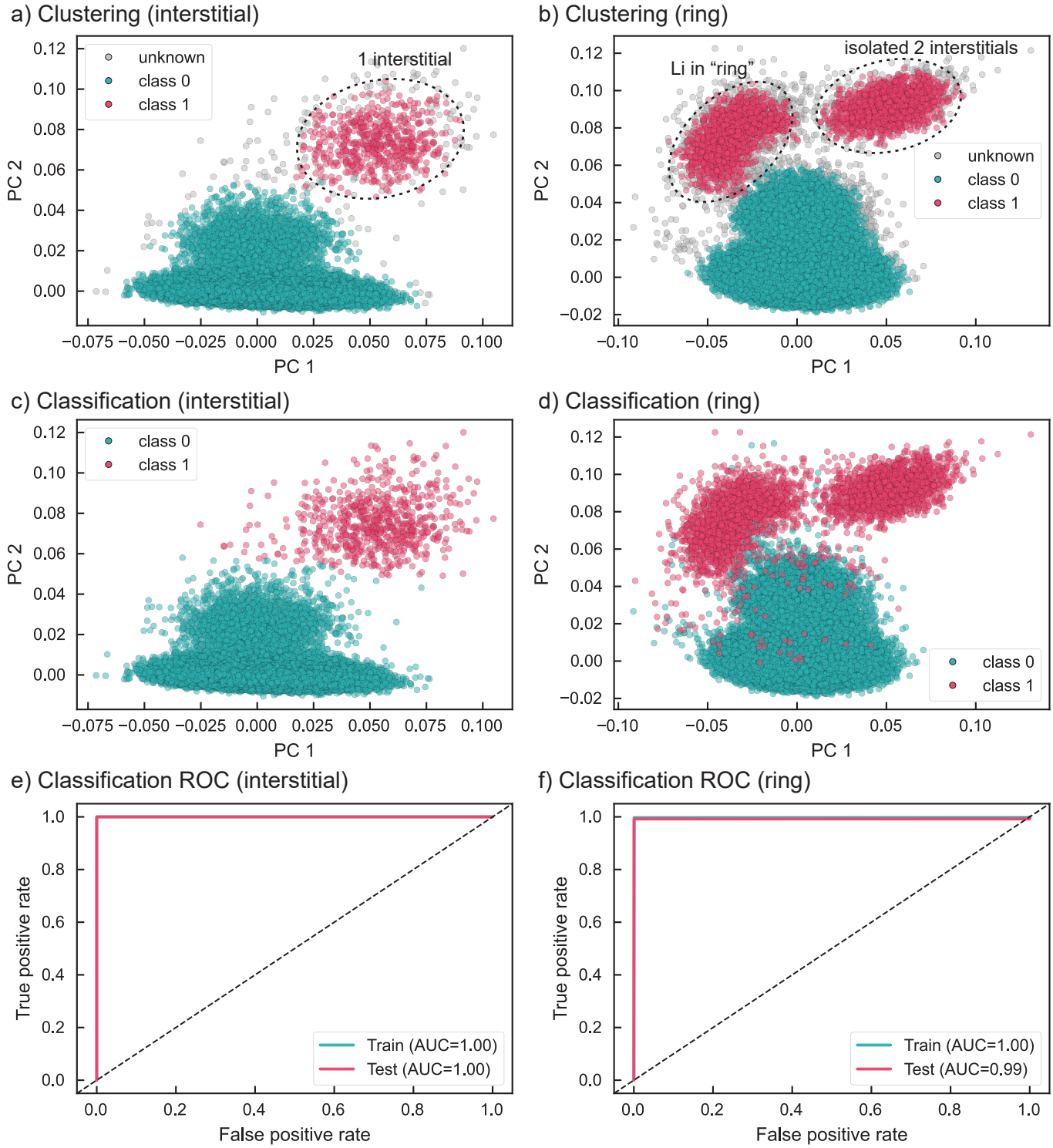



**Fig. S2:** Performance assessment of the SOAP-based classification algorithm. Results of the unsupervised DBSCAN clustering identifying Li in octahedral sites (class 0) and non-octahedral Li (class 1), namely interstitial Li (a) and ring-participating Li (b); gray points are unassigned (noise). For visualization, SOAP vectors are projected onto two dimensions using principal component analysis (PCA). Panels (c) and (d) show the output of the supervised classifier trained on the DBSCAN labels from (a). Receiver operating characteristic (ROC) curves for the training and test sets are shown in (e) and (f), with the area under the curve (AUC) values reported in the legend for identifying interstitial Li in (e) and the ring complex in (f).

**Table S1:** SOAP settings used for Li local-environment identification.

| Parameter | Value |
|---|---|
| SOAP cutoff radius $r_{\mathrm{cut}}$ | 6.0 Å |
| Gaussian width $\sigma$ | 0.3 Å |
| Maximum radial basis index $n_{\mathrm{max}}$ | 3 |
| Maximum angular index $l_{\mathrm{max}}$ | 2 |
| Weighting function | Polynomial |
| Weighting parameters | $r_0 = 4$, $m = 2$, $c = 1$, $d = 1$ |
| Chemical species | Li, F |
| Periodic boundary conditions | Yes |
| Averaging mode | Off |

These settings were chosen to provide a compact descriptor capable of distinguishing regular octahedral lithium environments from distorted non-octahedral configurations relevant to diffusion, while limiting feature dimensionality and computational cost.

# S2 Additional Analysis infos

## S2.1 MLIP: Validation

This section presents a further analysis of the reliability of the MLIP beyond the training and validation loss metrics reported in the main text. A set of complementary validation tests covering both local and bulk properties was collected.

Fig. S3 presents the parity analysis for energies and forces on the training and validation sets. Fig. S4 and S5 compare the MLIP with reference DFT for equilibrium and dynamical properties directly relevant to the diffusion study, including bulk phonon dispersion, the equation of state, and representative migration energy profiles.

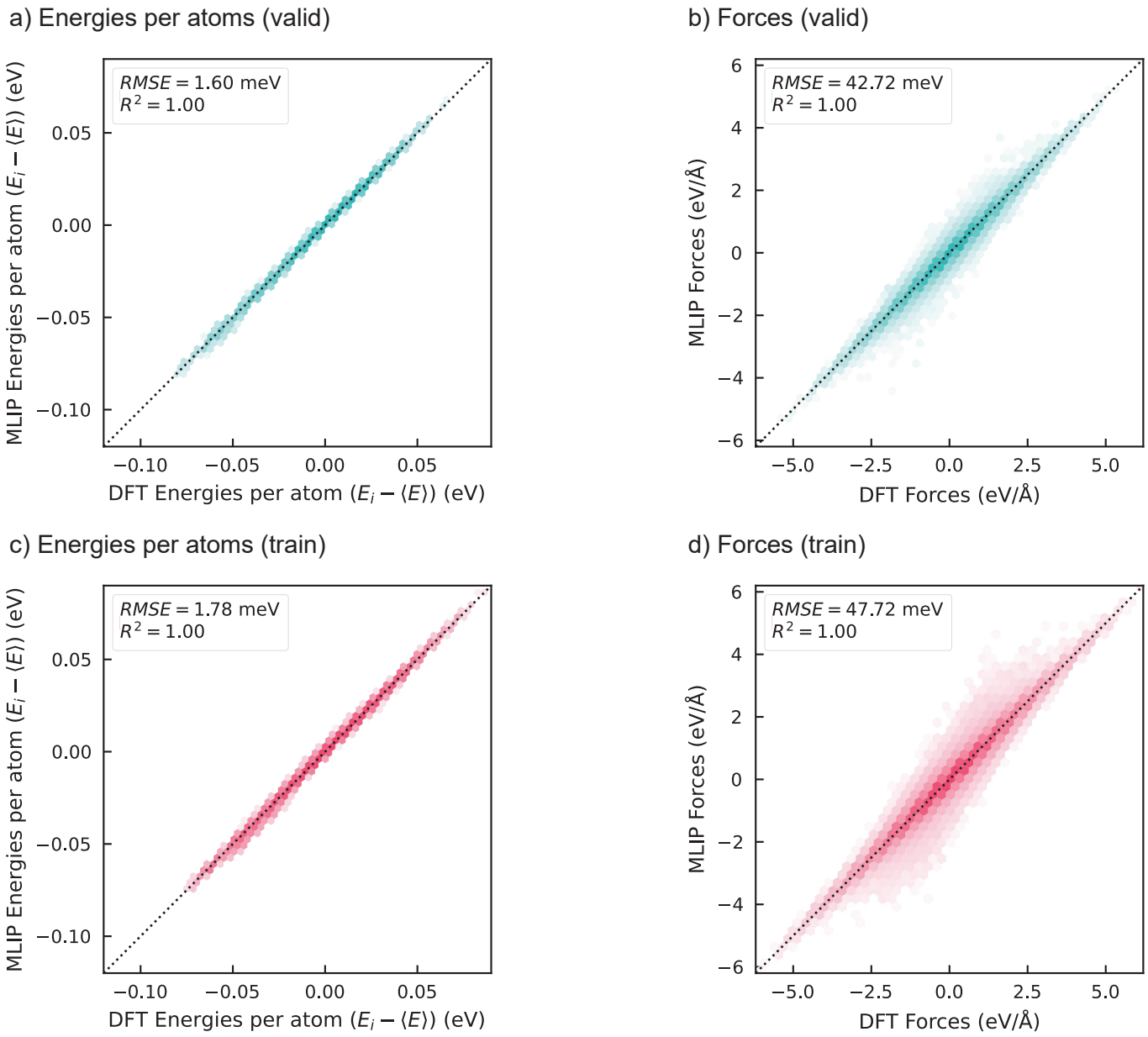



**Fig. S3:** MLIP validation: forces and energies for training and test sets. Parity plots of predicted energy per atom (left) and forces (right) against DFT, with the root-mean-square error ($RMSE$) and coefficient of determination ($R^2$) reported in the top-left corner, and the hexagonal bins are colored according to the logarithm of the number of data points in each bin. Plots show the analysis for the validation set (a, b) and the training set (c, d). Note: for energy per atom, $\langle E \rangle$ denotes the average energy of each system subset (bulk, 1 vacancy, 1 interstitial, 2 interstitials) and is subtracted to remove constant offsets arising from the defect formation energies.

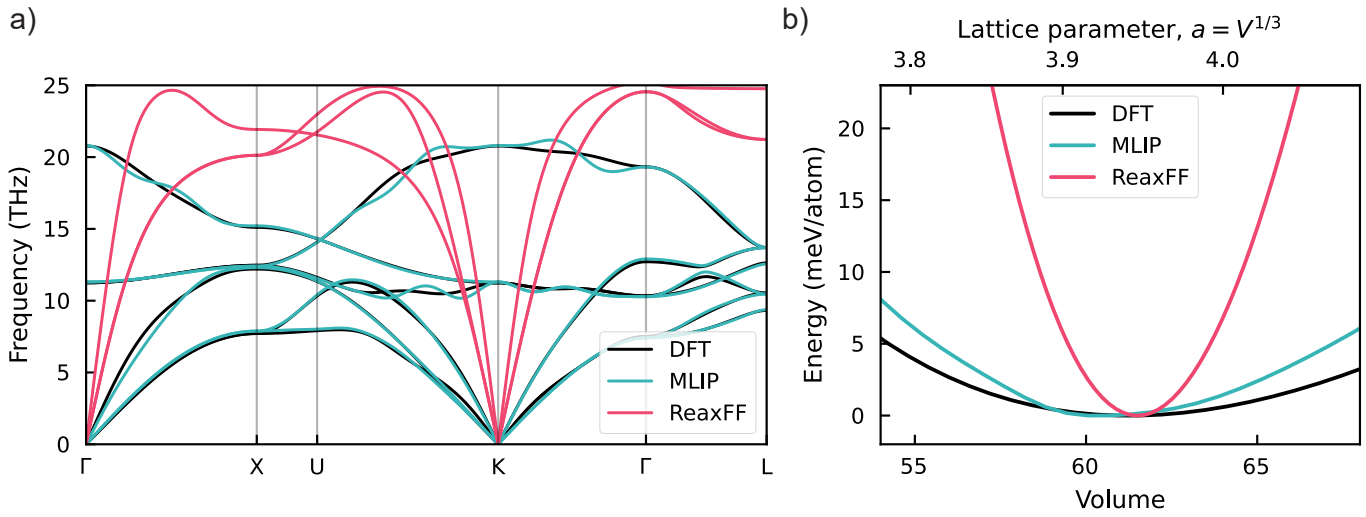



**Fig. S4:** MLIP validation for bulk LiF. (a) Phonon dispersion of the FCC LiF bulk structure obtained from reference DFT, MLIP, and ReaxFF [17]. (b) Equation of state obtained from reference DFT, MLIP, and ReaxFF [17]. Note that the MLIP was trained mainly around the equilibrium box size; the EOS could be further improved by including configurations at additional volumes in the training set.

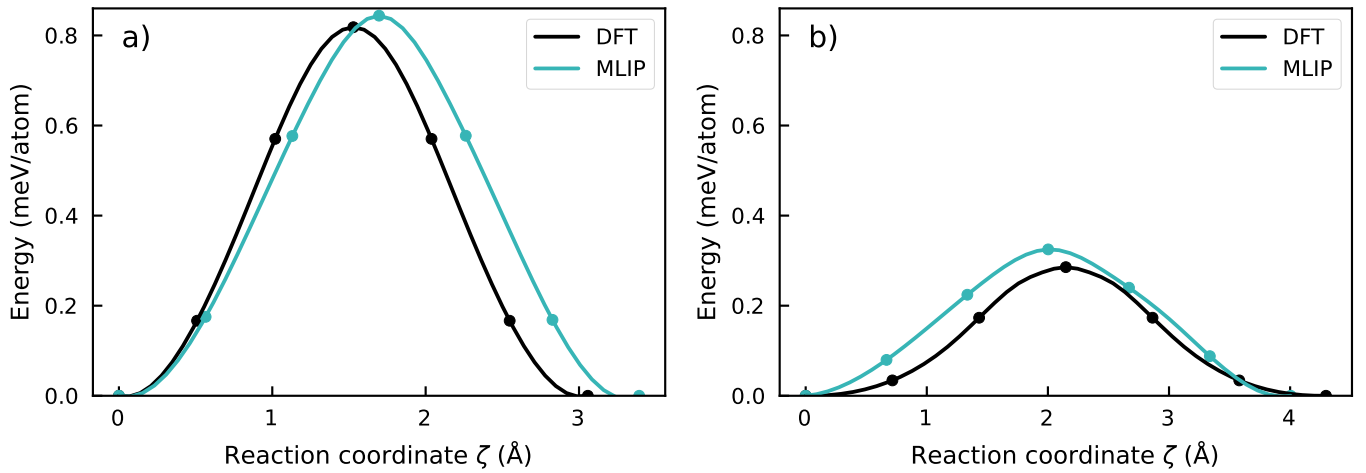



**Fig. S5:** MLIP validation: migration energy profiles. Nudged elastic band (NEB) simulations for vacancy diffusion along the (110) direction (a) and interstitial diffusion along the (110) direction, i.e. the knock-off mechanism (b), obtained with reference DFT and the MLIP. Small differences in shape are also influenced by the use of different NEB implementations in QE (DFT) and LAMMPS (MLIP).

## S2.2 Vacancy Diffusion: Finite size effect quantification and FES convergence

The robustness of the vacancy-diffusion free-energy analysis was quantified by examining finite-size effects and the time convergence of the OPES reconstruction. The finite-size comparison in Fig. S6 indicates that the vacancy migration barrier at 450 K remains consistent across $5 \times 5 \times 5$, $10 \times 10 \times 10$, and $15 \times 15 \times 15$ supercells. The time evolution of the collective variable, shown in Fig. S7, illustrates the accelerated sampling achieved in biased simulations at various temperatures. Additionally, Fig. S8 demonstrates the convergence of the reconstructed free energy surface with increasing simulation time, thereby supporting the reliability of the reported barrier values.

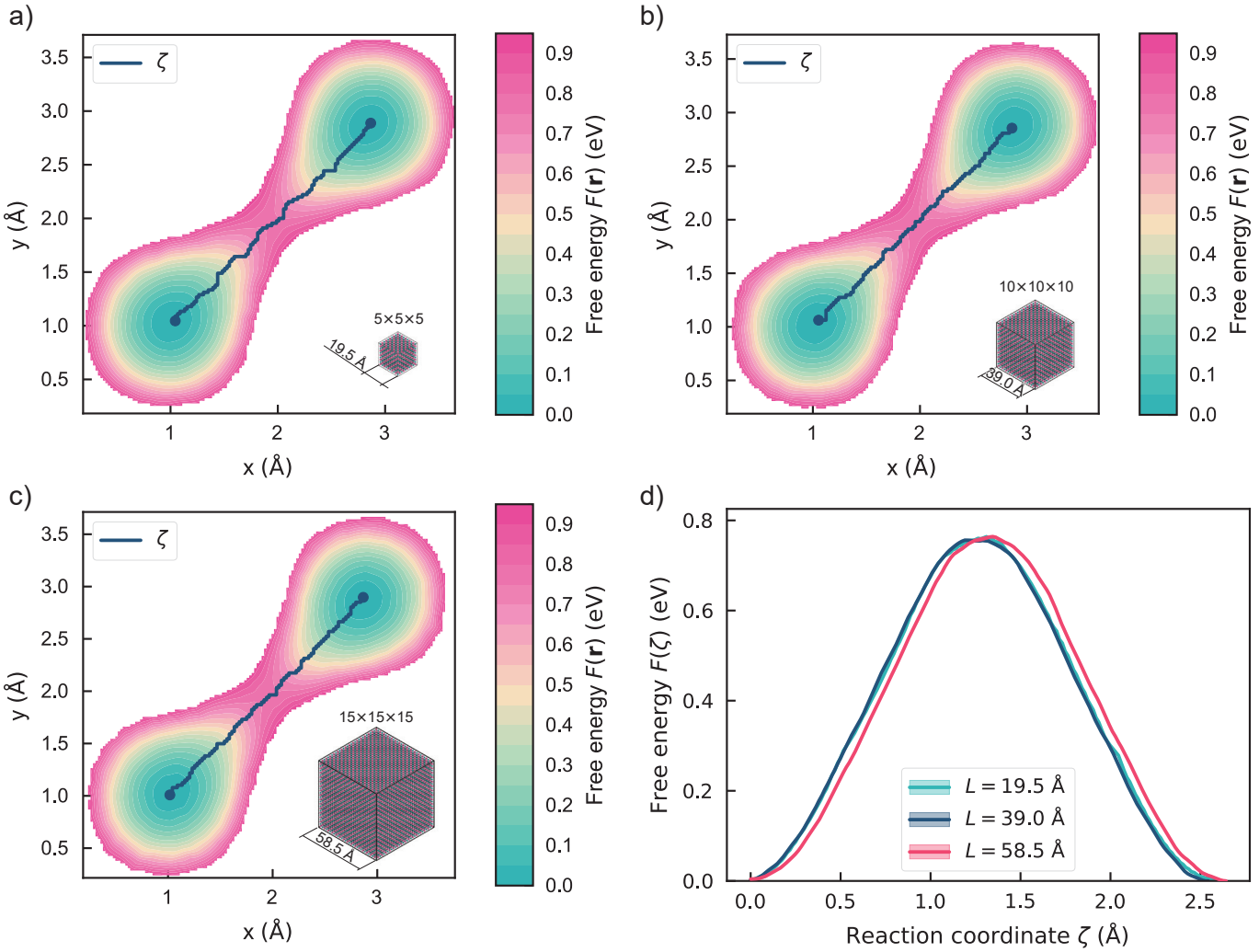



**Fig. S6:** Finite-size effect for vacancy diffusion. Free-energy surface obtained from OPES-biased simulations for vacancy diffusion at 450 K in three different supercells: (a) $5 \times 5 \times 5$, (b) $10 \times 10 \times 10$, and (c) $15 \times 15 \times 15$, corresponding to box lengths of 19.5 Å, 39 Å, and 58.5 Å, respectively. Panel (d)compares the free-energy barriers extracted from minimum-energy-path analysis (MEPSA), showing that the barrier height is invariant within uncertainty; the small differences in the reaction coordinate arise from the numerical path reconstruction.

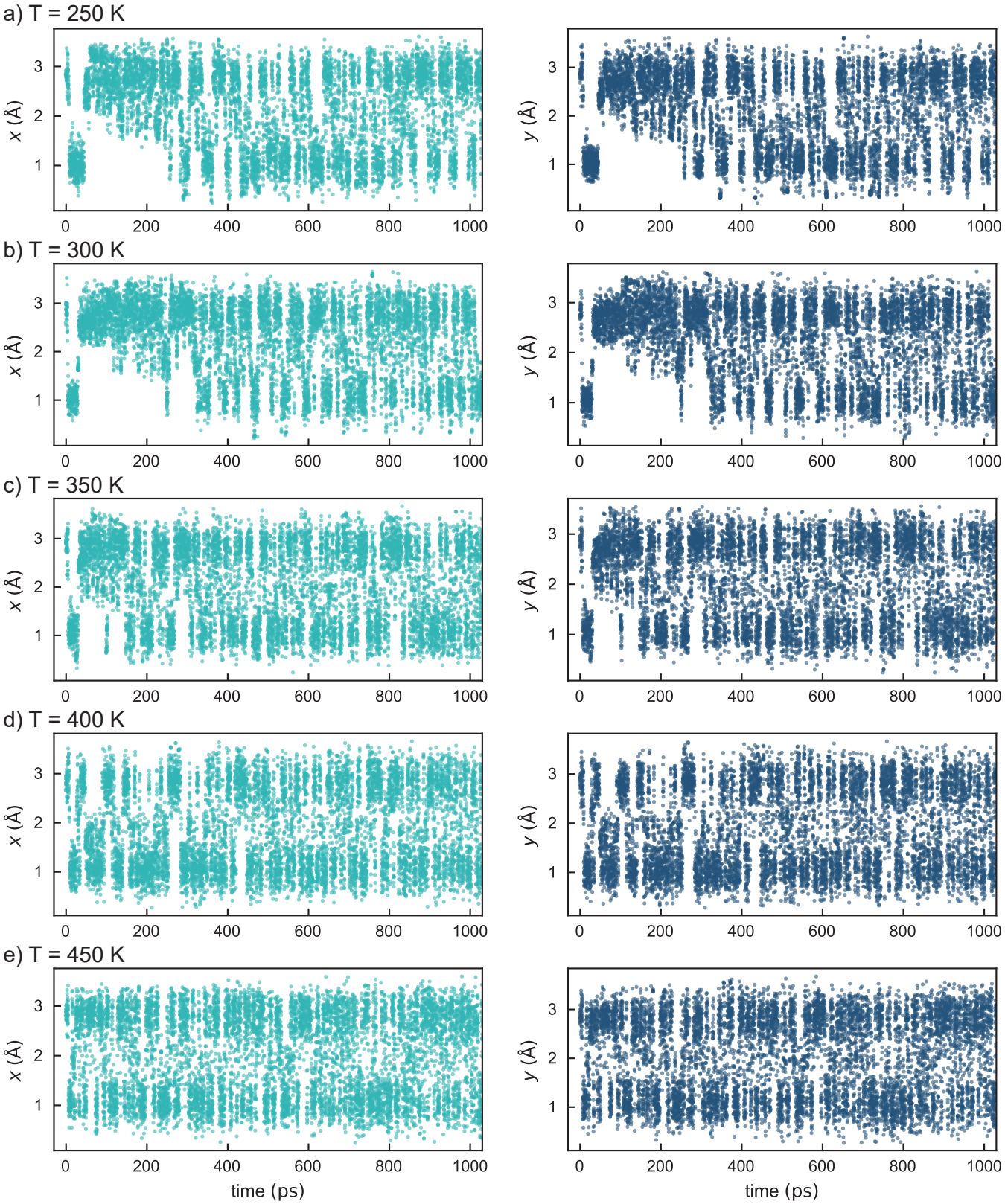



**Fig. S7:** Time evolution (restricted to the first 1 ns) of the collective variable ($x$, $y$ of Li atom) for the tagged Li atom in OPES-biased vacancy simulations at: (a) 250 K, (b) 300 K, (c) 350 K, (d) 400 K, (e) 450 K.

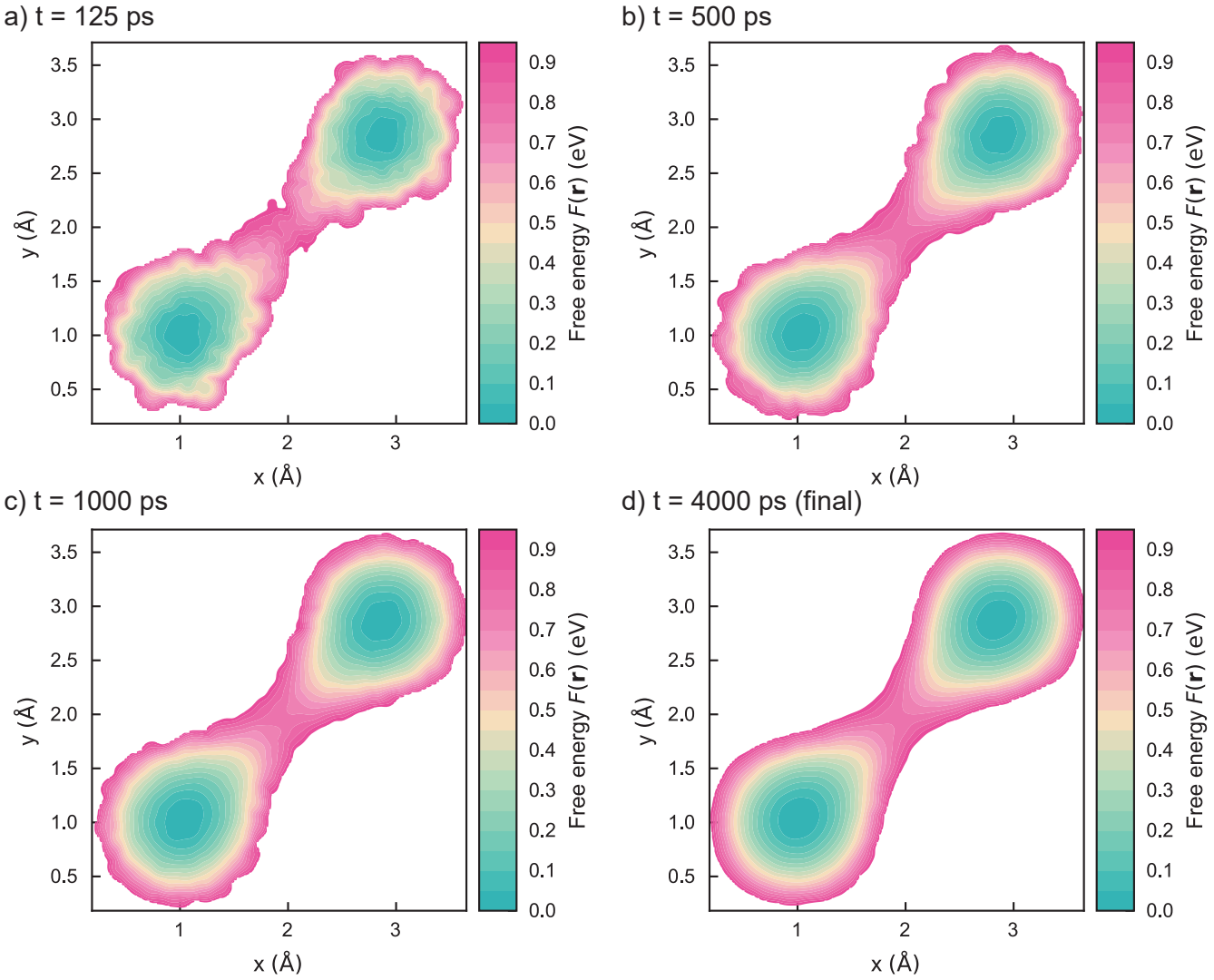



**Fig. S8:** Time convergence of the free-energy surface (FES). Two-dimensional FES in CV space at cumulative times: (a) 125 ps, (a) 500 ps, (a) 1000 ps, and (d) the final FES at 4 ns.

## S2.3 Interstitial Diffusion: Finite size effect quantification

To quantify possible finite-size effects in the single-interstitial diffusion analysis, we repeated the MLIP-MD simulations at 450 K using three supercells of increasing size: $5 \times 5 \times 5$, $10 \times 10 \times 10$, and $15 \times 15 \times 15$. The corresponding MSD curves and diffusivities are compared in Fig. S9. The overlap of the extracted diffusion coefficients within uncertainty shows that the single-interstitial diffusivity is not affected by the simulation cell size over the range considered here.

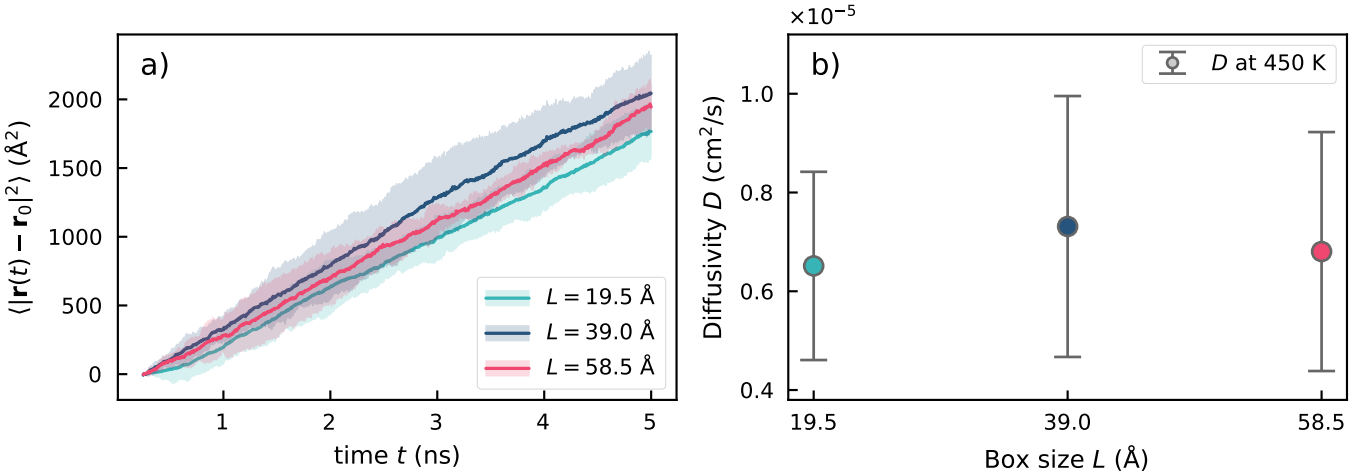



**Fig. S9:** Finite-size effect for single-interstitial diffusion. Mean-squared displacement (a) and corresponding diffusivity (b) for MLIP-MD simulations at 450 K with one interstitial Li, using three different supercells: $5 \times 5 \times 5$, $10 \times 10 \times 10$, and $15 \times 15 \times 15$ with box size 19.5 Å, 39 Å and 58.5 Å respectively.

## S2.4 Ring Diffusion: Additional Electronic-Structure Analysis

This section presents additional electronic-structure analyses supporting the interpretation of the ring configuration. Fig. S10 displays representative Bader-charge and frontier-orbital evidence related to ring formation, illustrating local valence-charge redistribution alongside the corresponding HOMO delocalization. Absolute Bader values may depend on the underlying real-space charge-density representation. Fig. S11 additionally reports a mesh-sensitivity test performed with increasingly dense FFT grids. The negligible variation observed confirms that the qualitative electronic-structure interpretation presented in the main text remains robust against charge-density discretization.

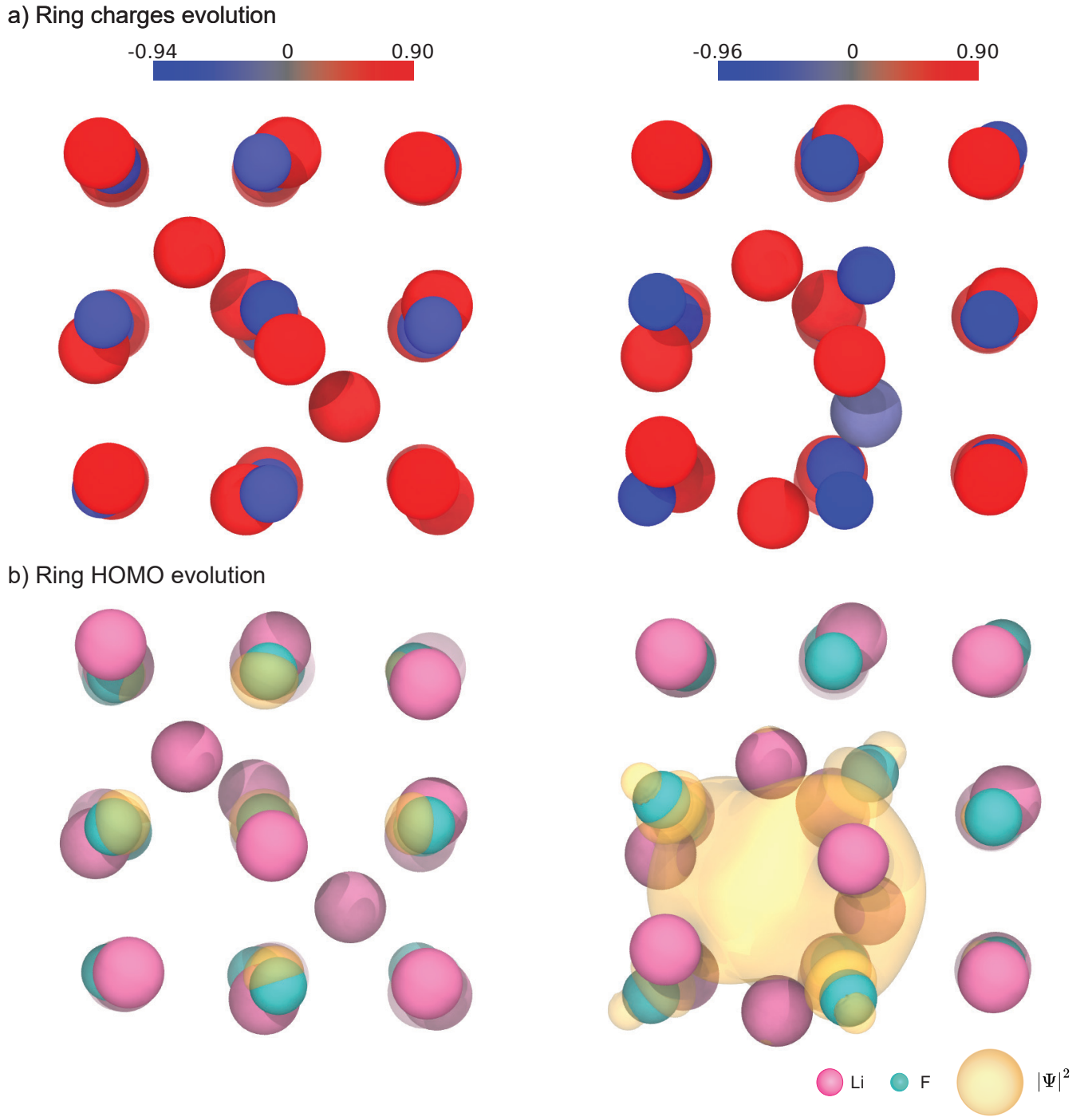



**Fig. S10:** Charge evolution during ring formation. (a) Bader-charge analysis (as in the main text) showing the partial redistribution of valence charge resulting in a reduced positive Bader charge of one Li atom when the six Li atoms arrange into the ring. (b) Isosurface of the HOMO electron probability density ($|\Psi|^2 = 0.001$) highlighting the electron delocalization consistent with the Li Bader-charge decrease in (a).

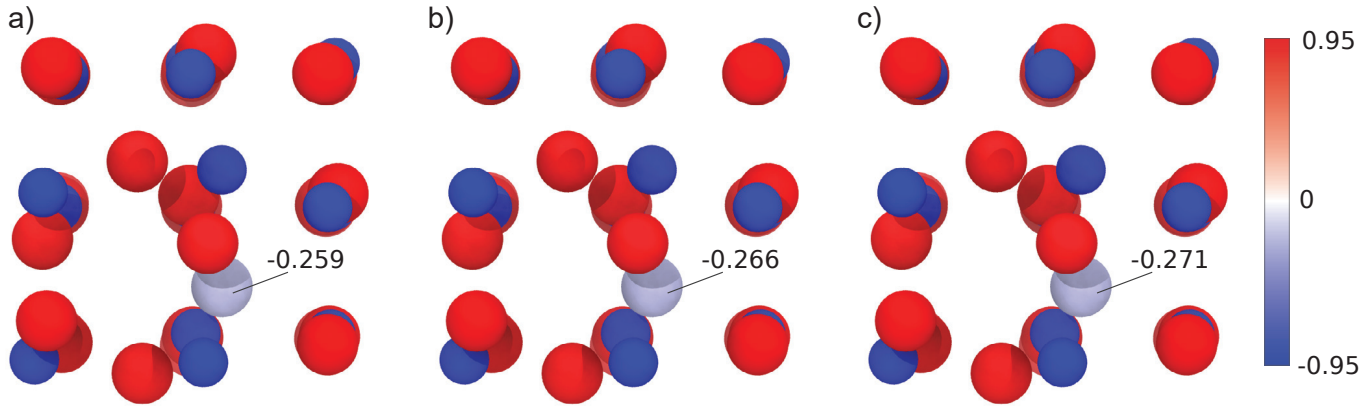



**Fig. S11:** Bader charge density grid sensitivity. Bader charges computed from single-point calculations using FFT meshes of (a) $150^3$, (b) $200^3$, and (c) $300^3$ points, corresponding to real-space spacings of 0.08 Å, 0.06 Å, and 0.04 Å, respectively (approximately equivalent to charge-density cutoffs `ecutrho` of 440 Ry, 770 Ry, and 1710 Ry). The negligible variation in the resulting Bader values confirms that the qualitative charge-redistribution trend discussed in the manuscript is insensitive to the FFT mesh density.

## S2.5 Ring Diffusion: Additional formation mechanism analysis

To clarify the origin of the ring mechanism, the dependence of the ring formation time, $\delta t_0$, on the simulation cell size was investigated.

For five supercells ($5\times5\times5$, $8\times8\times8$, $10\times10\times10$, $12\times12\times12$, and $15\times15\times15$), the formation time was measured across 16 independent unbiased replicas at 450 K. Figure S12 shows that $\delta t_0$ increases with box size following an approximately cubic scaling, i.e., $\delta t_0 \propto L^3$. Because the number of interstitials remains fixed while the simulation volume increases as $L^3$, this corresponds to an inverse proportionality with the effective interstitial concentration, $c$, such that

$$\langle \delta t_0 \cdot c \rangle = \text{const.} = (88 \pm 19)\,\text{ps mol L}^{-1} \tag{S15}$$

This result indicates that ring formation is governed by the time required for two interstitials to diffuse and encounter each other, rather than by any additional finite-size-specific mechanism.

The analysis was then extended to different temperatures to test whether the concentration-rescaled ring formation time follows activated behavior. Fig. S13 shows that the quantity $\langle \delta t_0 \cdot c \rangle$ follows an Arrhenius trend, expressed as

$$\langle \delta t_0 \cdot c \rangle = k_0 \exp\left(\frac{E_a}{k_B T}\right), \tag{S16}$$

or, equivalently, since $c$ is constant during each simulation,

$$\langle \delta t_0 \rangle = \frac{k_0}{c} \exp\left(\frac{E_a}{k_B T}\right). \tag{S17}$$

Linear interpolation of the $\ln(\delta t_0 \cdot c)$ versus $1/T$ plot yields an activation energy of $E_a = (0.230 \pm 0.015)$ eV and a prefactor $k_0 = (0.14 \pm 0.07)\,\text{ps mol L}^{-1}$. The $E_a$ value closely matches that obtained from the interstitial diffusion analysis presented in the main manuscript, supporting the interpretation that ring formation is governed by the same underlying lithium diffusion process, specifically the time required for interstitial migration and encounter.

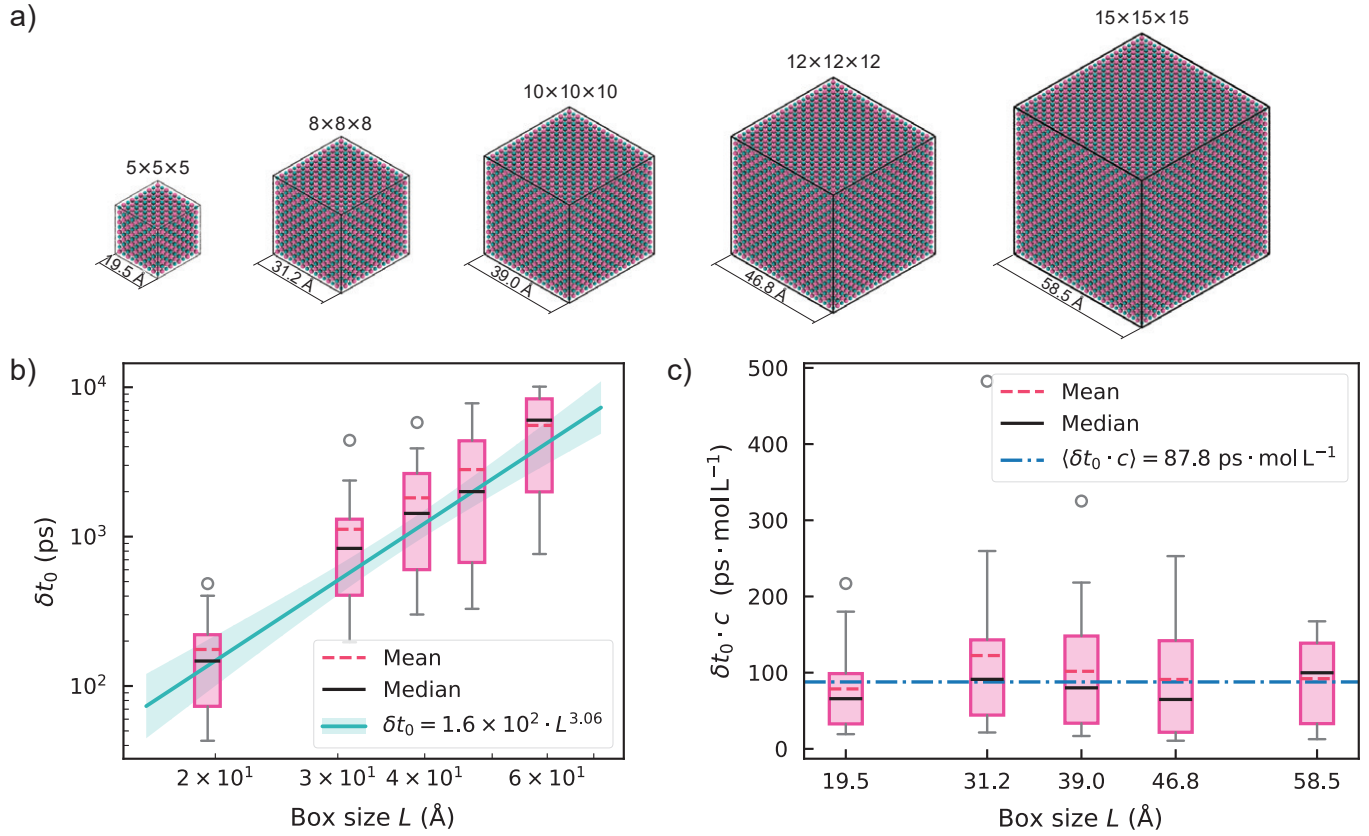



**Fig. S12:** Finite-size dependence of the ring formation time. Panel (b) displays a log-log plot showing that the ring formation time, $\delta t_0$, follows a cubic dependence on the box size, $L$, for the five supercells studied ($5 \times 5 \times 5$, $8 \times 8 \times 8$, $10 \times 10 \times 10$, $12 \times 12 \times 12$, and $15 \times 15 \times 15$), summarized in panel (a). Panel (c) shows the formation time rescaled by the effective Li interstitial concentration, $c$, confirming that the ensemble-averaged quantity $\langle \delta t_0 \cdot c \rangle$ is constant in all simulations.

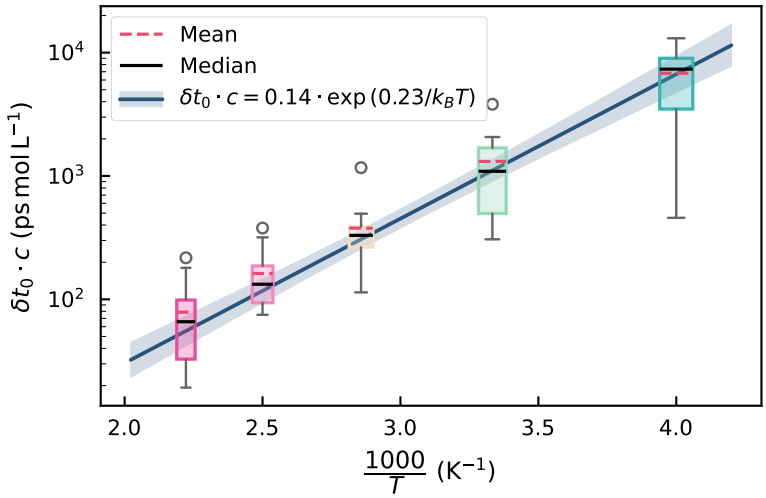



**Fig. S13:** Arrhenius plot for ring formation. The product $\delta t_0 \cdot c$ is shown to follow Arrhenius behavior, where $\delta t_0$ and $c$ represent the formation time and interstitial concentration, respectively.

## References


[1] F. Mambretti, U. Raucci, M. Yang, M. Parrinello, How Does Structural Disorder Impact Heterogeneous Catalysts? The Case of Ammonia Decomposition on Non-stoichiometric Lithium Imide, ACS Catalysis 14 (3) (2024) 1252–1256. doi:10.1021/acscatal.3c05376.
URL https://pubs.acs.org/doi/10.1021/acscatal.3c05376

[2] M. Invernizzi, M. Parrinello, Rethinking Metadynamics: From Bias Potentials to Probability Distributions, The Journal of Physical Chemistry Letters 11 (7) (2020) 2731–2736. doi:10.1021/acs.jpclett.0c00497.
URL https://pubs.acs.org/doi/10.1021/acs.jpclett.0c00497

[3] M. Invernizzi, M. Parrinello, Exploration vs Convergence Speed in Adaptive-Bias Enhanced Sampling, Journal of Chemical Theory and Computation 18 (6) (2022) 3988–3996. doi:10.1021/acs.jctc.2c00152.
URL https://pubs.acs.org/doi/10.1021/acs.jctc.2c00152

[4] A. Einstein, Über die von der molekularkinetischen Theorie der Wärme geforderte Bewegung von in ruhenden Flüssigkeiten suspendierten Teilchen, Annalen der Physik 322 (8) (1905) 549–560. doi:10.1002/andp.19053220806.
URL https://onlinelibrary.wiley.com/doi/10.1002/andp.19053220806

[5] M. Von Smoluchowski, Zur kinetischen Theorie der Brownschen Molekularbewegung und der Suspensionen, Annalen der Physik 326 (14) (1906) 756–780. doi:10.1002/andp.19063261405.
URL https://onlinelibrary.wiley.com/doi/10.1002/andp.19063261405

[6] M. P. Allen, D. J. Tildesley, Computer simulation of liquids, 2nd Edition, Oxford university press, 2017.

[7] H. Eyring, The Activated Complex in Chemical Reactions, The Journal of Chemical Physics 3 (2) (1935) 107–115. doi:10.1063/1.1749604.
URL https://pubs.aip.org/jcp/article/3/2/107/203352/The-Activated-Complex-in-Chemical-Reactions

[8] S. Arrhenius, ON THE REACTION VELOCITY OF THE INVERSION OF CANE SUGAR BY ACIDS, in: Selected Readings in Chemical Kinetics, Elsevier, 1967, pp. 31–35. doi:10.1016/B978-0-08-012344-8.50005-2.
URL https://linkinghub.elsevier.com/retrieve/pii/B9780080123448500052

[9] M. Abkenar, T. H. Gray, A. Zaccone, Dissociation rates from single-molecule pulling experiments under large thermal fluctuations or large applied force, Physical Review E 95 (4) (2017) 042413. doi:10.1103/PhysRevE.95.042413.
URL http://link.aps.org/doi/10.1103/PhysRevE.95.042413

[10] H. Kramers, Brownian motion in a field of force and the diffusion model of chemical reactions, Physica 7 (4) (1940) 284–304. doi:10.1016/S0031-8914(40)90098-2.
URL https://linkinghub.elsevier.com/retrieve/pii/S0031891440900982

[11] W. C. Navidi, Statistics for engineers and scientists, 5th Edition, McGraw-Hill Education, New York, NY, 2020.

[12] H. Yildirim, A. Kinaci, M. K. Y. Chan, J. P. Greeley, First-Principles Analysis of Defect Thermodynamics and Ion Transport in Inorganic SEI Compounds: LiF and NaF, ACS Applied Materials & Interfaces 7 (34) (2015) 18985–18996. doi:10.1021/acsami.5b02904.
URL https://pubs.acs.org/doi/10.1021/acsami.5b02904

[13] J. Zheng, Z. Ju, B. Zhang, J. Nai, T. Liu, Y. Liu, Q. Xie, W. Zhang, Y. Wang, X. Tao, Lithium ion diffusion mechanism on the inorganic components of the solid-electrolyte interphase, Journal of Materials Chemistry A 9 (16) (2021) 10251–10259. doi:10.1039/D0TA11444H.
URL https://xlink.rsc.org/?DOI=D0TA11444H

[14] S. De, A. P. Bartók, G. Csányi, M. Ceriotti, Comparing molecules and solids across structural and alchemical space, Physical Chemistry Chemical Physics 18 (20) (2016) 13754–13769. doi:10.1039/C6CP00415F.
URL https://xlink.rsc.org/?DOI=C6CP00415F

[15] L. Himanen, M. O. J. Jäger, E. V. Morooka, F. Federici Canova, Y. S. Ranawat, D. Z. Gao, P. Rinke, A. S. Foster, DScribe: Library of descriptors for machine learning in materials science, Computer Physics Communications 247 (2020) 106949. doi:10.1016/j.cpc.2019.106949.
URL https://doi.org/10.1016/j.cpc.2019.106949

[16] F. Pedregosa, G. Varoquaux, A. Gramfort, V. Michel, B. Thirion, O. Grisel, M. Blondel, P. Prettenhofer, R. Weiss, V. Dubourg, J. Vanderplas, A. Passos, D. Cournapeau, M. Brucher, M. Perrot, E. Duchesnay, Scikit-learn: Machine learning in Python, Journal of Machine Learning Research 12 (2011) 2825–2830.

[17] P. De Angelis, R. Cappabianca, M. Fasano, P. Asinari, E. Chiavazzo, Enhancing ReaxFF for molecular dynamics simulations of lithium-ion batteries: an interactive reparameterization protocol, Scientific Reports 14 (1) (2024) 978. doi:10.1038/s41598-023-50978-5.
URL https://www.nature.com/articles/s41598-023-50978-5